

Performance of an Automatic Detector and Locator Tested on Synthetic Seismograms

A Case Study from Litoměřice in Czech Republic

Eva Káldy  * ¹, Tomáš Fischer  ¹

¹Institute of Hydrogeology, Engineering Geology and Applied Geophysics, Faculty of Science, Charles University, Albertov 6, Prague, 120 00, Czech Republic

Author contributions: *Conceptualization:* Eva Káldy, Tomáš Fischer. *Methodology:* Eva Káldy. *Software:* Tomáš Fischer, Eva Káldy. *Formal Analysis:* Eva Káldy. *Writing - Original draft:* Eva Káldy. *Writing - Review & Editing:* Eva Káldy, Tomáš Fischer. *Funding acquisition:* Tomáš Fischer.

Abstract Seismic network sensitivity and event detection performance are critical for assessing earthquake risks, particularly in regions susceptible to induced seismicity. In seismically inactive zones, the network monitoring presents unique challenges, even when using adapted automated detection and location systems originally designed for active zones. In this study, we evaluate the capabilities of the seismic network deployed in the Litoměřice region of the Czech Republic, where a geothermal project is underway; no seismicity has been recorded in the area during years of monitoring. Using synthetic seismograms, we simulate potential earthquakes in the geothermal well to assess the network's detection efficiency in the area of interest. PEPiN (Polarization based Earthquake Picker for Networks) is employed to analyze the synthetic dataset with real background seismicity. Our results demonstrate that PEPiN detects and localizes 82% of the synthetic events with magnitude of completeness M_L -0.5, slightly above the value M_L -0.7 predicted by our previous research (Káldy and Fischer, 2023). Overall, our findings provide valuable insights into the seismic monitoring capabilities of the Litoměřice network, shedding light on the potential strengths and limitations of seismic surveillance systems in similar geothermal and underground operation settings.

Production Editor:
Gareth Funning
Handling Editor:
Lise Retailleau
Copy & Layout Editor:
Théa Ragon

Signed reviewer(s):
Ezgi Karasozen

Received:
May 6, 2024
Accepted:
March 21, 2025
Published:
April 9, 2025

1 Introduction

Induced or triggered seismicity stemming from various industrial operations, such as geothermal power plants (Deichmann and Giardini, 2009), CO₂ storage (White and Foxall, 2016), mining activities (Dubiński et al., 2019), and shale gas and oil extractions (Clarke et al., 2014; Grigoli et al., 2018), has been observed to affect public areas and private buildings, sometimes leading to damage. Consequently, as a precautionary measure, future projects are subjected to seismic monitoring in order to enable adjustments to the underground operations in the event of escalating seismic activity (Majer et al., 2012; Kraft et al., 2020). Typically, long-term monitoring entails the deployment of a network of surface seismic stations surrounding the operational facility; shallow or deep borehole sensors are used infrequently. Analysis of the recorded seismograms allows for the identification of ongoing seismicity (Fischer, 2003b; Perol et al., 2018; Doubravová and Horálek, 2019). Detected earthquakes (seismic events) are then located and assigned magnitudes. The resulting seismic catalog offers insights into the spatial and temporal characteristics of the activity, and can be characterized in terms of minimum and completeness magnitudes, which are indicative of the network's sensitivity (Wiemer and Wyss, 2000; Káldy and Fischer, 2023). The sensitivity of the network depends on factors such as station network geometry, noise levels and coupling,

underground geological conditions, depth and distance of earthquakes, and the detection method used, even in cases where the catalog has no events (Hallo, 2012; Káldy and Fischer, 2023).

Recently, automated detection methods have improved with the integration of machine learning techniques such as Convolutional Neural Networks (CNN) (Giudicepietro et al., 2017; Magrini et al., 2020; Stepnov et al., 2021). These detection systems now exceed the capabilities of the more traditional detection methods, such as matched filtering using both real (Janská and Eisner, 2012; Gibbons and Ringdal, 2006) and synthetic templates (Chamberlain and Townend, 2018), as well as comparisons of short-term and long-term STA/LTA ratios (Allen, 1978, 1982; Velasco et al., 2016), enhanced with polarity filters to identify P and S wave arrivals (Fischer, 2003b, method PEPiN presented here), among other techniques. Evaluation of the resulting detection catalogs can include metrics such as the magnitude of completeness (M_C) that occurs as it deviates from the Gutenberg-Richter law (Wiemer and Wyss, 2000; Leptokaropoulos and Gkarlaouni, 2016), the minimal detectable magnitude (M_m) (Káldy and Fischer, 2023; Yang et al., 2021), the false event ratio, and the accuracy of earthquake locations. M_C (or M_m) can also be simulated and presented as the seismic network sensitivity, which depends on factors such as network size (number of stations, distances, and geometry), distance from the earthquake, noise levels, geological condi-

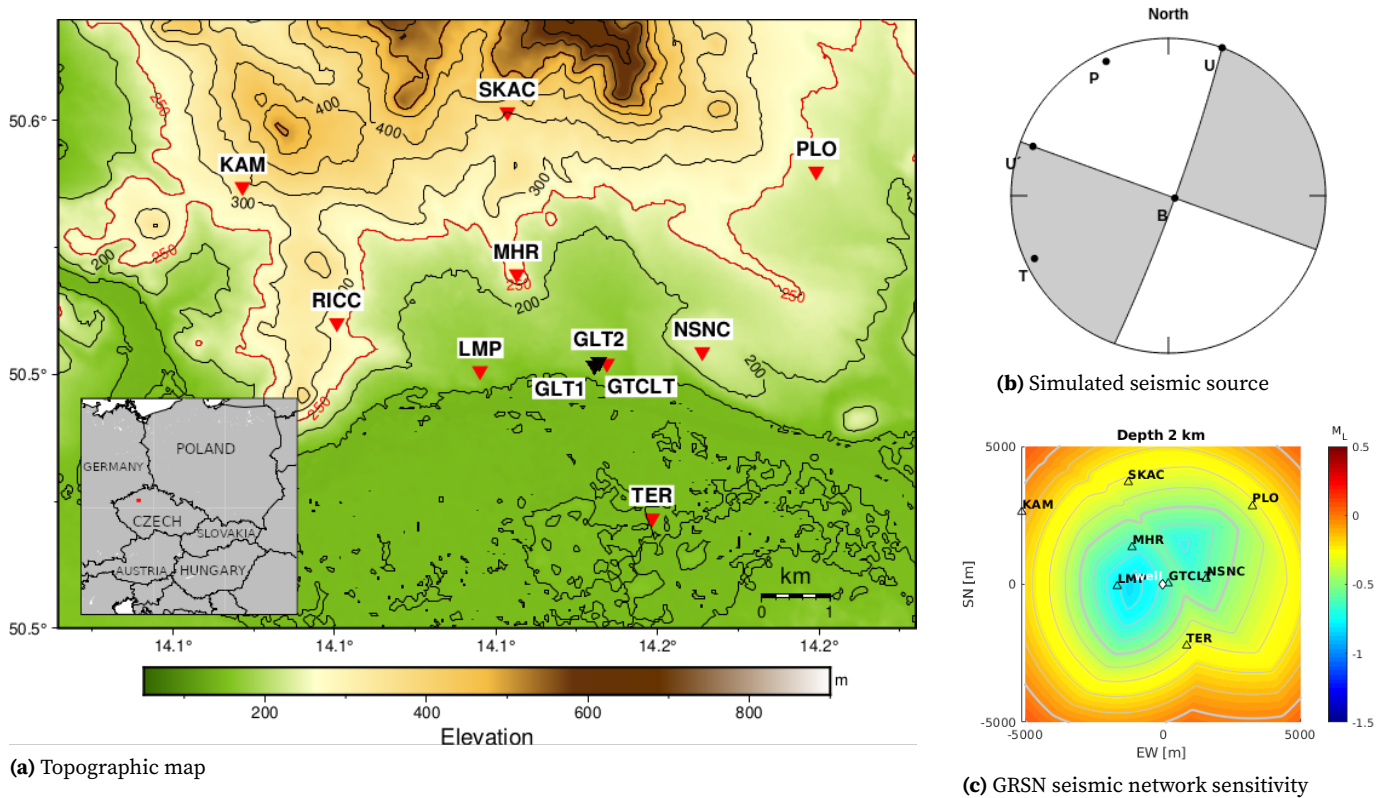


Figure 1 GRSN local seismic network in Litoměřice, Czech Republic, Europe. (a) Topographic map with stations’ locations noted by triangles and names; red triangles for surface stations, black for stations in wells. 4 surface stations are located at the base rock (KAM, RICC, SKAC, MHR - baserock stations) and lie within the brownish area above the 250 m isoline. Stations located atop horizontally layered sediments of the Bohemian Cretaceous Basin (LMP, GLT1, GLT2, GTCLT, NSNC, TER, PLO - sedimentary stations) are in the greenish low-land area. The EGS is expected to take place at a borehole near station GLT1 at a depth of 2 km. (b) Focal mechanism of the simulated seismic source below GLT1 station: strike 20, dip 85, rake 0, depth 2 km), M_W 1. (c) GRSN seismic network sensitivity, provided where 4 stations are required for the event detection. Horizontal cross-section at depth 2 km in terms of magnitude completeness M_C . Figure (b) adopted from Káldy and Fischer (2023).

tions, and the applied automated detection algorithms (Káldy and Fischer, 2023; D’Alessandro et al., 2011; Wilson et al., 2021). Simulated network sensitivity can be compared to existing detection catalogs or tested using synthetic earthquakes (López-Comino et al., 2017) when real earthquakes are not detected, as is the case presented here. The advantage of analyzing detector performance on synthetic records is that the real completeness of the M_C and interpreted b -values can be debated (Leptokaropoulos et al., 2018).

The seismically inactive Litoměřice region in the Czech Republic presents an intriguing opportunity to assess the applicability of an automated seismic detector and locator, PEPiN (Polarization based Earthquake Picker for Networks), which was originally tailored for the West Bohemia region (Fischer, 2003b), where it demonstrated detection capabilities with M_C -0.7 at a 6 km depth and M_C -0.3 at an 11 km depth (Káldy and Fischer, 2023) for 8 stations of the WEBNET seismic network (Institute of Geophysics, Academy of Sciences of the Czech Republic, 1991, epicentral distance 0 - 15 km). Since 2019, the Litoměřice region has been monitored by the Geothermal Research Seismic Network (GRSN) (Šafanda et al., 2020; Káldy and Fischer, 2023, Fig. 1a), primarily to ensure the safety of an emerging geothermal project (Šafanda et al., 2020, project Ringen/Syn-

ergys). This enhanced geothermal system (EGS) benefits positively from the fact that no seismic events have been detected in the region down to a magnitude of completeness M_L -0.7 at the depth 2 km at the well site when using 8 surface stations (Káldy and Fischer, 2023). The GRSN network, as of Autumn 2023, was comprised of 11 stations, including 9 surface stations (stations RICC and NSNC were in shallow underground locations), and 2 located within wells (station GLT1 at 1500 m and station GLT2 at 190 m below the surface), equipped with a mix of broad-band and short-period receivers (broad-band receivers at stations KAM, RICC, TER, PLO, and SKAC, short-period receivers at stations LMP, MHR, NSNC, and GTCLT). The Litoměřice region is geologically segmented (Šafanda et al., 2020), with 7 stations situated amidst semi-horizontally layered sediments of the Bohemian Cretaceous Basin and 4 stations at bedrock outcrops of older formations, predominantly the Central Bohemian Volcanic Complex. Accordingly, stations are categorized into sedimentary and baserock groups, demarcated by the 250 m elevation contour line (highlighted in red) in Fig. 1a.

This article extends the previous research on GRSN network sensitivity (Káldy and Fischer, 2023) by conducting reliability tests using synthetic earthquakes overlaid onto real seismic records. The theoretical net-

work sensitivity from the preceding study is shown in terms of the M_C variation at a depth of 2 km in Fig. 1c: only the stations denoted by black triangles were considered for the detection, assuming an event is detected when a minimum of 4 stations receive the S wave signal exceeding (3 times representative) noise. In Fig. 1c, the light blue color west of the well location (white diamond) represents the area of the greatest network sensitivity at the depth where water is likely to be injected during the EGS project; thus, the weakest earthquake that can confidently be detected at a depth of 2 km is $M_L-0.85$, or $M_L-0.7$ at the well location.

To test the performance of the PEPiN detection and location algorithm for potential EGS-induced seismicity in Litoměřice, we created nearly-realistic daily seismograms simulating earthquakes below one of the borehole stations (GLT1). The aim is to provide PEPiN seismograms including challenges such as noise increase during the day, noise bursts, P and S arrivals not explainable by a homogeneous velocity model, the potential for false phase picking particularly on converted waves, and the variation in polarities and amplitudes among stations due to focal mechanisms. To achieve this objective, recorded noise is overlaid by 2880 synthetic seismograms of various magnitudes, but of similar location and focal mechanism. Event magnitudes were randomly distributed throughout the day, adhering to the Gutenberg-Richter law with a b -value of 1.5. This chosen b -value is consistent with the established range of $1 < b < 2.1$ for induced seismicity, as documented by Geffers et al. (2022) and Muntendam-Bos and Grobbe (2022). Similar waveforms of the simulated seismic activity are used to resemble the real case scenario of induced events in Basel (Kraft and Deichmann, 2014). Changes in the underground geology (sediment vs. hardrock) are incorporated via two 1D velocity models in order to provide some variation in the expected arrival times in an inhomogeneous environment. Finally, the real records of all the GRSN stations are collected during a typical working day, which provides the temporal and typological variations in noise.

In the subsequent sections, we will delve into the methodologies employed in generating synthetic seismograms, introduce the automated detector and locator PEPiN, discuss the results obtained when detecting synthetic events in real noise, and draw comparisons with the simulated network sensitivity established by Káldy and Fischer (2023). Through this comprehensive analysis, we aim to refine our understanding of PEPiN's applicability in the Litoměřice region and contribute to the broader discourse on seismic monitoring in low-seismicity regions.

2 Methodology: Synthetic seismograms

Simplistic synthetic seismogram can consist of single P and S wave peaks at expected arrival times. Realistic variations and complexity in seismic waveforms appear to be more suitable for assessing detection techniques since detection-location engines may fail to recognize

or match correct phases. Generating more advanced synthetic seismograms is a complex process (Shearer, 2009) with its core being the Green's functions (GF). The GFs represent Earth's response to unit impulsive point loads, covering all the elastic Earth properties and boundary conditions. Initially, seismic source parameters such as location, focal mechanism, and magnitude are set to match the most likely scenario. Subsequently, the seismic wave propagation is simulated using numerical, ray tracing, homogeneous layer, normal-mode or semi-analytical methods (Shearer, 2009; Wang et al., 2017); each utilizes the best available Earth's structural model. The resulting space derivatives of Green's functions are then convolved with the seismic source time function to produce synthetic seismograms at each station. Additionally, the instrument response and site effects may be incorporated into the synthetic seismograms to enhance their conformity to the observed data. It is worth noting that the proximity of earthquakes increases the frequency of the seismic record, necessitating detailed underground information for accurate simulation (Levin et al., 2010).

Seismogram modeling can address the variations in the Earth's elastic parameters and density in all three dimensions, although modeling solely in one dimension reduces the processing time significantly. Given that most of the seismic stations in Litoměřice are situated atop the sedimentary Bohemian Cretaceous Basin (borehole: GLT1, GLT2; surface: GTCLT, LTM, NSNC, PLO and TER; Fig 1a), a predominantly horizontally layered media (Uličný et al., 2009), a 1D velocity model is adequate for these "sediment stations".

In contrast, four of the eleven seismic stations in the Litoměřice area (KAM, MHR, RICC and SKAC; Fig. 1a) are located atop the baserocks of the Central Bohemian Volcanic Complex (Cajz et al., 2009; Mysliveček et al., 2018), bordering the Bohemian Cretaceous Basin. Such a geological setting makes the use of a single 1D earth model unjustifiable, and if realistic synthetic seismograms can be calculated, a 3D model would be more beneficial. For testing the detection reliability it is sufficient that the synthetic waveforms vary not just in wave arrival times but also in waveform shape and complexity, referring to different geological basements. An additional 1D baserock velocity model, reflecting Earth parameters encountered by seismic rays arriving at the "baserock stations", provides the required waveform variation and, as such, also provides a 3D effect to the study. While the representation of this baserock model is limited, the resulting synthetic seismograms provide variations in the waveforms and phase arrival times suitable for testing the performance of a detection-location engine.

2.1 1D velocity models

Creating synthetic seismograms necessitates a robust velocity model. In the Litoměřice region, a particular attention is given to depths up to 3 km; the EGS project will likely inject the water to a depth of 2 km. To account for the major geological features of the area, two velocity models were compiled for this study: sedimen-

Formation	depth km	V_p km/s	V_s km/s	ρ g/cm ³	Q_p	Q_s
Surface sediments	-0.171	1.2	0.7	1.8	30	13
	0.025	2.0	1.2	1.8	30	13
Cretaceous siltstone	0.025	2.2	1.3	2.3	58	26
	0.19	2.3	1.4	2.3	58	26
Permocarbon siltstone	0.19	2.5	1.5	2.46	70	31
	0.78	4.1	2.4	2.61	150	67
Permocarbon porphyr	0.78	4.6	2.7	2.81	500	222
	0.95	4.6	2.7	2.81	500	222
Proterozoic gneiss	0.95	6.0	3.5	2.82	500	222
	2.7	6.1	3.6	2.82	500	222
Granite	2.7	6.2	3.6	2.66	1000	444
	8.0	6.3	3.7	2.82	1100	489

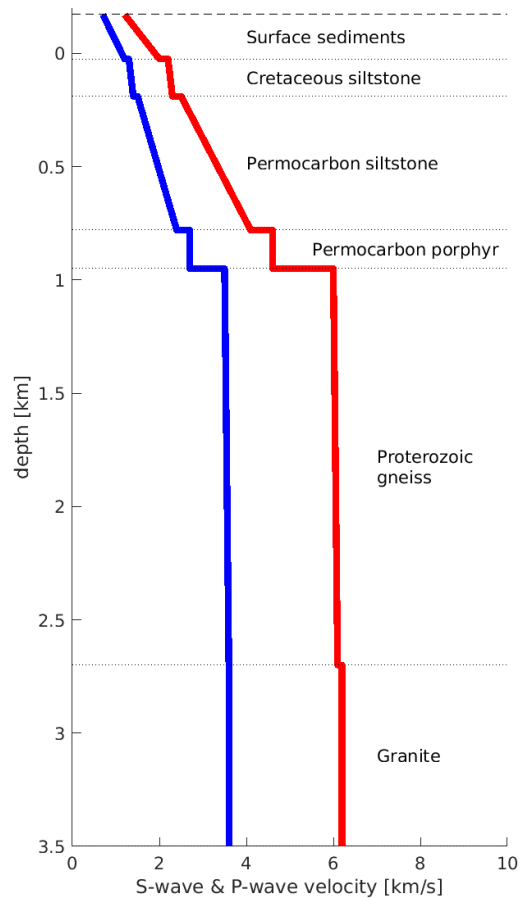
Table 1 Layered sedimentary 1D velocity model representing the Bohemian Cretaceous Basin in Litoměřice, Czech Republic.

tary velocity model for the Bohemian Cretaceous Basin (sedimentary area) and baserock velocity model for the stations located atop the hardrock of a volcanic body or a limestone (baserock area).

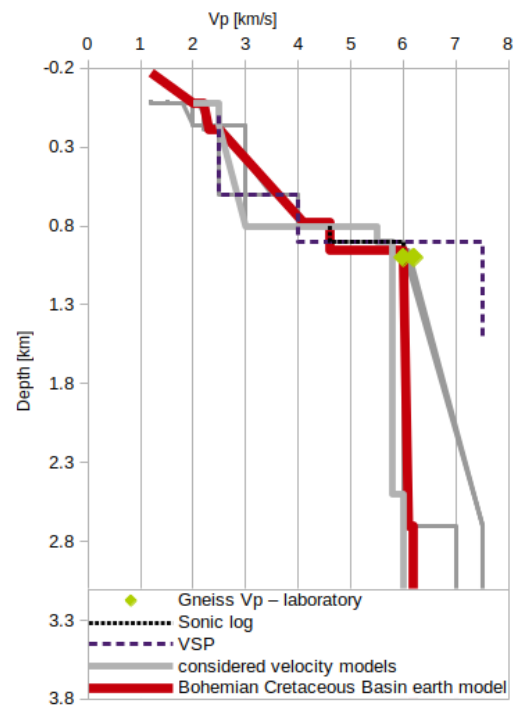
The sedimentary velocity model is an outcome of this study and comprises six layers, with two layers exhibiting a significant gradient increase in parameters. Tab. 1 gives a detailed list of all parameters in the Litoměřice sedimentary velocity model. Additionally, Fig. 2a illustrates the corresponding velocity profile, providing further insights into its structure and composition. Fig. 2b shows the level of uncertainties in the sedimentary velocity model based on the available measurements and considered velocity profiles. And there is a ray-path through the sedimentary layers drawn in blue in Fig. 3.

The velocities of the sedimentary model down to a depth of 2 km are derived from geological profiles and core descriptions obtained from the 2111 m deep pilot well PVGT-LT1 (Burda et al., 2008). Velocities for greater depths are extrapolated from the reinterpreted north-south section of the borehole and the Litoměřice geothermal structure (Myslil et al., 2012). Bedrock densities are determined from geophysical interpretations of the geological profile Cínovec – Mělník (Myslil et al., 2007), while attenuation factors Q_p and Q_s are based on publicly available data and values utilized in West Bohemia, Czech Republic (Bachura, 2017). The resulting P wave velocity model is calibrated to align with vertical seismic profile (VSP) measurements down to 1500 m (measured in July 2019, personal communication with J. Vilhelm), acoustic logs at depths of 850 to 1050 m (Kasza et al., 2007), and laboratory velocity measurements on gneiss samples from a depth of 1100 m (T. Lokajíček, personal communication). The standard 1.7 ratio between P and S wave velocities is maintained throughout the profile, validated by previously conducted laboratory measurements (T. Lokajíček, personal communication). The velocity model uncertainties are not quantified but the variations in experienced and tested velocities are shown in Fig. 2b.

For seismic stations situated on baserock, the base-



(a) Velocity model



(b) Uncertainty in velocity model

Figure 2 Velocity profile at the EGS location. (a) 1D P and S wave velocity profile of Bohemian Cretaceous Basin (sedimentary area) in Litoměřice. V_p [km/s] in red, V_s [km/s] in blue, corresponding to Tab. 1. (b) Various P wave velocities from local measurements (VSP, sonic log and laboratory) utilized for creating the final 1D earth model (red line - similar to V_p in (a)). Gray lines represent some of the tested velocity profiles.

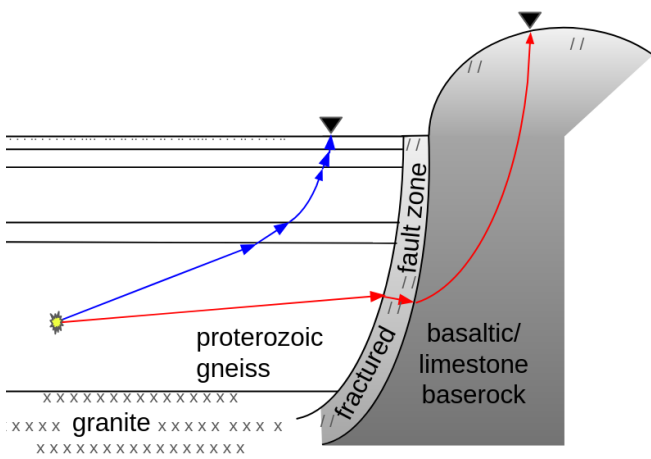


Figure 3 Sketch of the geological structure in the Litoměřice region. The sedimentary area, shown on the left, is separated from the baserock area on the right by a regional fault. The seismic source (yellow) is located at a depth of 2 km within Proterozoic gneiss. The red line with arrows depicts the seismic ray path from the source to a seismic station atop the baserock formation, corresponding to the 1D baserock velocity model outlined in Tab. 2. The blue line represents the seismic ray path from the source to a station above the sedimentary layers, corresponding to the velocity model described in Tab. 1.

rock 1D velocity model represents velocities and densities along the expected ray path from the synthetic source to the baserock stations. It is based on the previously described sedimentary velocity model, optimized for the seismic source at a depth of 2 km. It is anticipated that the seismic wave originates at a depth of 2 km in the Proterozoic gneiss, where it travels horizontally, encounters the brittle Litoměřice Fault Zone (Šafanda et al., 2020), passes through the high velocities of a volcanic body or limestone, and finally traverses an eroded layer, volcanoclastic material, and upper sedimentary layers (Cajz et al., 2009, <https://mapy.geology.cz/geocr50/>), see the red ray-path in Fig. 3. The uncertainty associated with seismic rays encountering volcanic structures is addressed by incorporating parameters that exhibit gradient increases with depth for baserock and that are decreasing with depth for the fault zone (Tab. 2). Although this baserock velocity model is a reasonable approximation of the geology likely to be encountered by the seismic signal between the source at GLT1 at 2 km and receivers at baserocks, it does not represent any real vertical geological profile (no basalts over sediments in the Litoměřice region). While this 1D baserock model serves as a valuable tool for testing detection-location algorithms by adding variation in waveform shape and complexity, its applicability is primarily within the scope of this project.

2.2 Generating synthetic seismograms

A synthetic seismogram depicts a theoretical ground motion at a specific location corresponding to a theoretical earthquake, defined by its focal mechanism, magnitude, and location. Seismograms for all stations in

Formation	depth km	V_p km/s	V_s km/s	ρ g/cm ³	Q_p	Q_s
Base rock	-0.31	4.0	2.4	2.0	500	222
Fractured	0.95	6.4	3.8	3.0	500	222
Proterozoic gneiss	1.1	6.0	3.5	2.82	500	222
	2.7	6.1	3.6	2.82	500	222
Granite	2.7	6.2	3.6	2.66	1000	444
	8.0	6.3	3.7	2.82	1100	489

Table 2 The baserock 1D velocity model represents the velocities encountered by the seismic ray originating at a depth of 2 km in the Bohemian Cretaceous Basin (sedimentary area) and arriving at a station located atop the Central Bohemian Volcanic Complex (baserock area). Refer to the red ray path in Fig. 3.

the GRSN network in Litoměřice are simulated using the open-source seismology toolbox and library Pyrocko by Heimann et al. (2017, 2019, 2020).

Fomosto, the manager for Pyrocko’s Green’s functions (GF), offers multiple backends suitable for different scales and expected outcomes. We calculated the GF using the numerical QSEIS backend given by Wang (1999), based on a layered viscoelastic half-space velocity models. Grid parameters and sampling rates were carefully chosen to avoid aliasing in both time and space. A large number of reflected, converted, P and S phases are tabulated to enhance the complexity of the produced seismogram. The resulting GFs for surface receivers atop the sedimentary basin is one of the outcomes of this paper and the Green’s function store is available.

Using these GFs, Pyrocko allows the simulation of multiple types of point and finite seismic sources and various source time functions. For scaling the amplitude, the moment magnitude

$$M_w = \frac{2}{3} (\log M_0 - 9.1) \tag{1}$$

(Hanks and Kanamori, 1979, M_0 in Nm) is used. The corresponding ground motion can be delivered either in terms of displacement or velocity. Using a double-couple point source to describe the shear ruptures, the source time function of a unit pulse response is representative of an induced shallow event in the Litoměřice region; the focal mechanism and event location is depicted in Fig. 1b. Waveforms in ground velocity are generated to match the recorded velocigrams.

3 Methodology: PEPiN - detection and location algorithm

The PEPiN detection and location algorithm (Polarization based Earthquake Picker for Networks) was developed with the aim of detecting earthquakes recorded by the WEBNET seismic network (Institute of Geophysics, Academy of Sciences of the Czech Republic, 1991) in the earthquake swarm region of West Bohemia in Czechia. This algorithm stems from the automatic picker and locator (Fischer, 2003b) applied on the data of the 2000

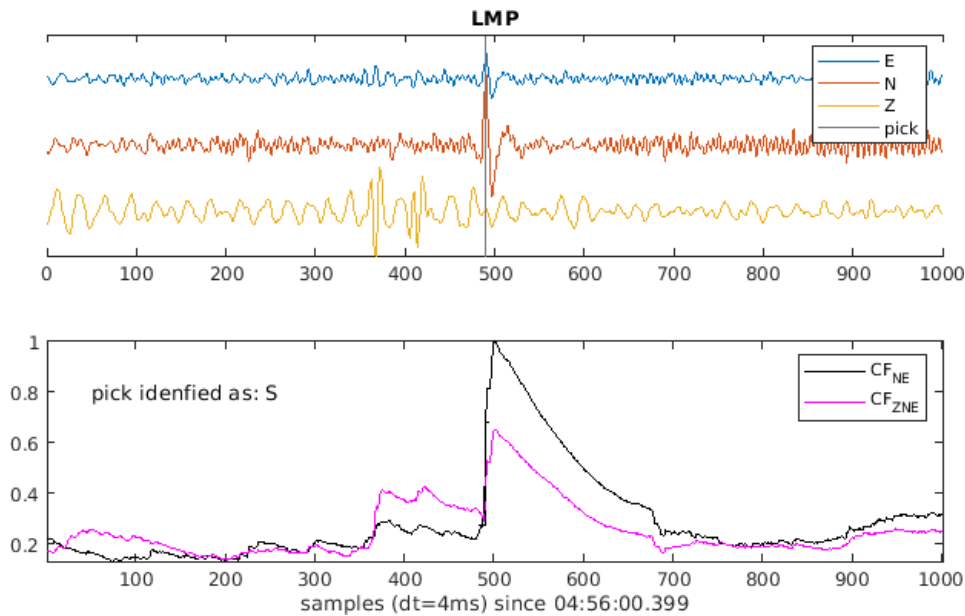


Figure 4 Picking process in PEPiN. A noisy three-component seismogram (station LMP, filtered 7-30 Hz) of a small local earthquake (top) with corresponding characteristic functions (CF) used for phase detection and picking (bottom).

swarm in this area (Fischer, 2003a) and is coded in Matlab. PEPiN now operates in near-real time at the WEBNET and GRSN seismic network and it has also been successfully applied to the continuous data from the Reykjanet seismic network deployed on the Reykjanes Peninsula in Iceland (Fischer et al., 2022).

PEPiN consists of two independent components, a phase picker and a phase associator, which also provides preliminary locations of the detected events.

The picker produces a large number of candidate arrival times, which enables a broad choice of suitable data for the phase associator. The picker works on three component waveforms, which are converted to the characteristic function (CF) that amplifies the coherent signal (Allen, 1978). To this purpose, we use polarization-based CF in terms of the maximum eigenvalue of the signal covariance matrix; this highlights the signal, which is correlated among components (Mago-tra et al., 1987). The characteristic function

$$[CF]_{ab} = \frac{\sigma_{aa} + \sigma_{bb} + \sqrt{(\sigma_{aa} - \sigma_{bb})^2 + 4\sigma_{ab}^2}}{2\sqrt{\sigma_{aa} + \sigma_{bb}}} \quad (2)$$

is computed for each pair of components (a, b) in a moving window where a and b stands for the North, East and vertical components and σ is the covariance. In this way, the horizontal eigenvalue CF_{NE} and the vertical eigenvalue $CF_{ZNE} = 1/2(CF_{ZN} + CF_{ZE})$ are obtained. Local maxima for the CF_{NE} and CF_{ZNE} are then identified with mutual time intervals above a specified threshold and are then passed to the STA/LTA detector with non-overlapping time windows (Fischer, 2003b) to obtain the arrival time pick that precedes the relevant maximum. In parallel, the maximum vector amplitude of horizontal components, the STA/LTA ratio and the halfwidth of the envelope of the three-component signal are recorded. Fig. 4 shows the three-component seismogram of a small earthquake and the characteristic function series in the horizontal and ver-

tical plane; a dominant pick is identified and recognized as an S wave.

The phase associator aims to assign phase detections at different stations to a single event, working primarily with P or S waves depending on their signal strength in the region. To achieve this, the PEPiN associator employs kinematic criteria related to the seismic network geometry (assuming similar station altitude) to choose the correct phases and to form a seismic event. The input of the associator works with phase times and amplitudes and the weight of being a P or S phase, which is based on the polarization incidence angle cosine (Rosenberger, 2010). The associator searches for the consistent combination of arrival times using the criterion of the maximum permitted time difference between the chosen master phase (P or S) at stations and the maximum event depth that constrains the maximum difference between the S and P arrival times. Phases of all stations are joined in a single time series and events are defined as phase groups with time differences of consecutive master phases lower than the maximum permitted master phase time difference between stations. Because the above-defined phase groups may contain more master phases per station, time consistency measures are applied to choose the most suitable master phase for each station. Then, further phase types (S or P) are searched for, either after or prior to each valid master phase in a time window derived from the network aperture. A Wadati diagram is applied to find the most suitable further phase in the case where multiple candidate further phases exist and to exclude possible outliers. Preliminary locations of detected earthquakes are obtained using a non-linear grid-search optimization (Fischer, 2003a). Outliers are also removed during the location procedure by iteratively skipping phase picks with the highest residuals until the location RMS decreases below a specified threshold.

In the case of locally induced earthquakes in the Lito-

station	SKAC	RICC	NSNC	MHR	TER	PLO	LMP	KAM	GTCLT	GLT1	GLT2
C_i	-0.346	0.2	0.398	-0.508	0.083	0.093	0.196	0.017	0.067	0.95	0.82

Table 3 Station correction C_i for stations of the local seismic Litoměřice network GRSN, derived from regional earthquakes (extended table to Káldy and Fischer, 2023).

měřice region, the master phase is the S wave since the GRSN network is expected to record stronger S waves than P waves. Therefore, PEPiN is set up to declare an event when at least 4 S waves coincide; the number four being rather conservative. A single additional P wave is then required for the event to be assigned the preliminary location; consequently, the number of detected and located events might vary slightly. Location is performed with a homogeneous velocity model of P wave velocity 5.9 m/s and V_p/V_s 1.7. Prior PEPiN is executed, the seismograms are band-pass filtered at 7-30 Hz.

3.1 Local vs. moment magnitude

The basis of this project is that every synthetic event detected (and located) is characterized by two distinct magnitude scales (M_W and M_L). M_W is assigned when generating synthetic seismograms. M_L is determined by PEPiN from its hypocentral distance and the maximum S wave amplitude according to Jakoubková (2018), utilizing the station corrections given in Tab. 3. There is an empirical relationship between M_L and the seismic moment M_0 : $\log M_0 = 1.12M_L + 9.78$ (Horálek and Šílený, 2013) derived for the West Bohemia region, where a similar M_L formula is applied. A combination of the above and Equation 1 by Hanks and Kanamori (1979) leads to a theoretical relationship:

$$M_L = 1.34M_W - 0.61 \quad (3)$$

This relationship is later compared to the experimental data, resulting in an updated relationship between M_W and M_L , see below. This new relationship is then used to convert the M_W of synthetic seismograms to the M_L in order to represent the results in a consistent manner.

4 Results: Performance test on synthetic seismograms

The performance of the PEPiN algorithm is tested on real noise records overlaid by 2880 synthetic events at similar locations and focal mechanisms (Fig. 1), but at various magnitudes. PEPiN is evaluated in terms of detection and location efficiency.

Initially, the efficiency of the PEPiN detection algorithm was tested on 8 surface GRSN stations to compare with the predicted network sensitivity as outlined by Káldy and Fischer (2023), which refers to similar 8 stations. Furthermore, the performance of PEPiN, including all 9 surface and 2 borehole receivers, was evaluated in a subsequent analysis phase. If the need arises, the performance of PEPiN might also be tested on more station subsets, as was done in the previous study by Káldy and Fischer (2023), but this is not currently within the scope of this work.

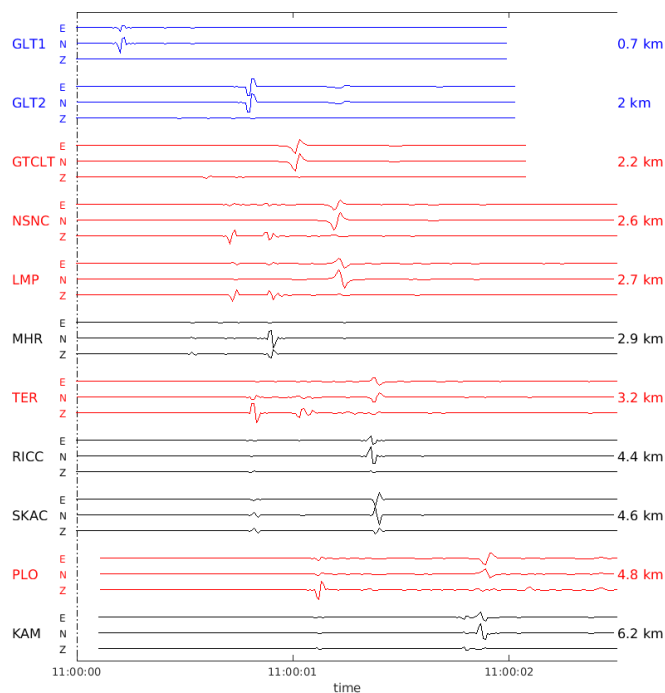


Figure 5 Synthetic seismograms. East (E), North (N) and vertical (Z) components of synthetic ground velocity seismograms for all seismic stations of the GRSN seismic network. Blue represents borehole receivers, red the surface receivers at the sedimentary basin, black for receivers on top of a base rock formation. The origin time is indicated by the black dashed line. The hypocentral distance is given on the right. No real seismic data (noise) is added in this display, no filter is applied, and the individual scale is per station.

4.1 Synthetic seismograms

A synthetic seismogram was created for this study, representing a potentially induced seismic event occurring during EGS at a 2 km depth at the GLT1 location. The methods used are described in the section [Generating synthetic seismograms](#); the focal mechanism is visualized in Fig. 1b. The resulting synthetic seismograms (Fig. 5) show mostly clear P and S wave arrivals, occasionally accompanied by reflected and converted waves as well as numerical noise. The synthetic seismogram record at the borehole receiver GLT1 (located in the same velocity layer as the source, only 678 m away) shows a single S wave peak at the expected time; the P wave amplitude is present but negligible due to the proximity of the nodal plane. Similar results are seen at the second borehole receiver GLT2 (Fig. 5). More distant surface stations at the sedimentary basin, such as NSNC or TER, exhibit two significant P wave arrivals, the second being recognized as an upward S wave converted to a P wave at the deeper porphyritic interface. The SP

wave shows a reverse polarity compared to the direct P wave arrival, due to transmission from the higher to the lower velocity medium (Kennett and Furumura, 2019; Nolte and Tsoflias, 2021). Overall, the synthetic seismograms representing a potential induced earthquake in the Litoměřice region exhibit sufficient complexity to pose challenges for automatic detection and location algorithms.

Synthetic events of similar waveforms (Fig. 5) but different magnitudes were introduced into the real seismic records at intervals of every half-minute, resulting in a total of 2880 events per day. The amplitudes of these synthetic events were adjusted to correspond to magnitudes respecting the Gutenberg-Richter distribution law with a *b*-value of 1.5; event magnitudes were randomly distributed throughout the day. The span of magnitudes is also set to conveniently represent the detection results in terms of minimal detectable magnitude, varying for tests on 8 or 11 stations. Consequently, two sets of daily seismograms are used - similar in terms of noise, varying in terms of overlaid synthetic events.

4.2 Magnitude conversion to M_L

Verification of the theoretical relationship between M_W and M_L (Eq. 3) is conducted by comparing the M_W prescribed to synthetics and the M_L measured by PEPiN (Fig. 6a), resulting in the best fit equation of

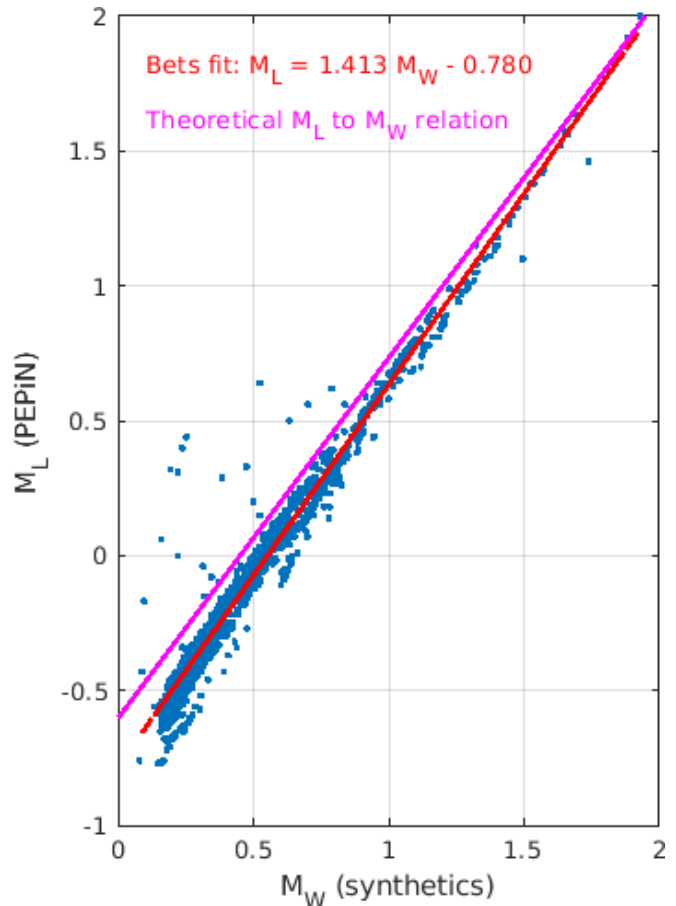
$$M_L = 1.41M_W - 0.78 \tag{4}$$

which is closely aligned with the theoretical scaling (Eq. 3). This best-fit relation (Eq. 4) is used to convert M_W to M_L for transparent result presentation. It also ensures consistency with previous studies (Káldy and Fischer, 2023; Jakoubková, 2018) and is more suitable since M_W is typically not used for smaller earthquakes, despite Horálek and Šílený (2013) assertion of the lack of a straightforward link between WEBNET M_L and moment magnitude M_W . As a consequence of the M_W to M_L conversion, the magnitude range of the synthetic seismogram shifts and the *b*-value is perturbed as well: from 1.44 to 1.04 (Fig. 6b).

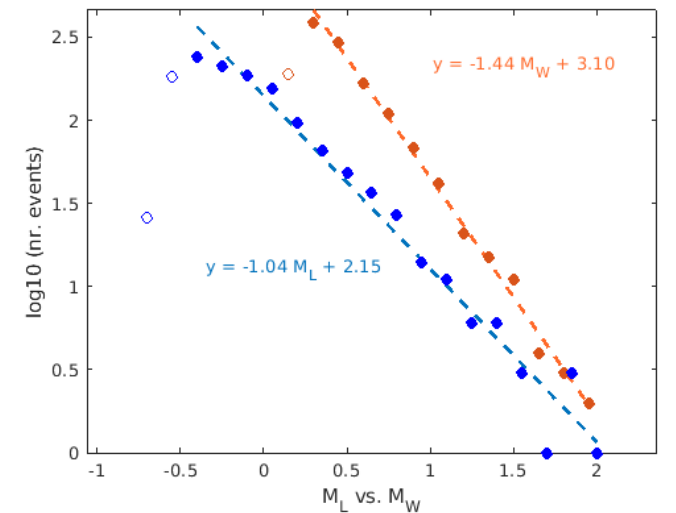
4.3 Detection efficiency

The PEPiN detection efficiency in the GRSN network is tested on a real seismic record overlaid with thousands of synthetic seismograms varying in magnitude but constant in waveform shape. The events detected by PEPiN are associated with the synthetic ones and only the M_L derived from M_W (Eq. 4) is published. The synthetic dataset varies in magnitude for tests conducted with either 8 or 11 GRSN stations, while maintaining a similar background seismic signal. Results of PEPiN the detection efficiency with 8 surface and 9 surface + 2 borehole stations are discussed.

It is noteworthy that all the recognized wave arrivals are associated with the correct phases, with a single exception observed on KAM due to an unusual S wave arrival. Also note that the P and S arrivals in Fig. 10 do not fully correlate with the epicentral distance: the wave arrivals at sedimentary stations (red waveforms) are later



(a)



(b)

Figure 6 Local magnitude M_L and moment magnitude M_W of events detected by PEPiN at 8 surface stations. (a) Theoretical (magenta, Eq. 3) vs. best fit relationship (red, Eq. 4) for all the events (blue points) detected and located by PEPiN at 8 stations. (b) Gutenberg-Richter magnitude - frequency distribution - in the prescribed M_W of synthetics (orange) and in M_L derived by PEPiN (blue). The maximum of the distribution (first filled point from left) is interpreted as the magnitude of completeness M_C : M_{LC} -0.4, M_{WC} 0.3. Linear fitting of filled points gives the *b*-value: 1.04 for M_L , 1.44 for M_W .

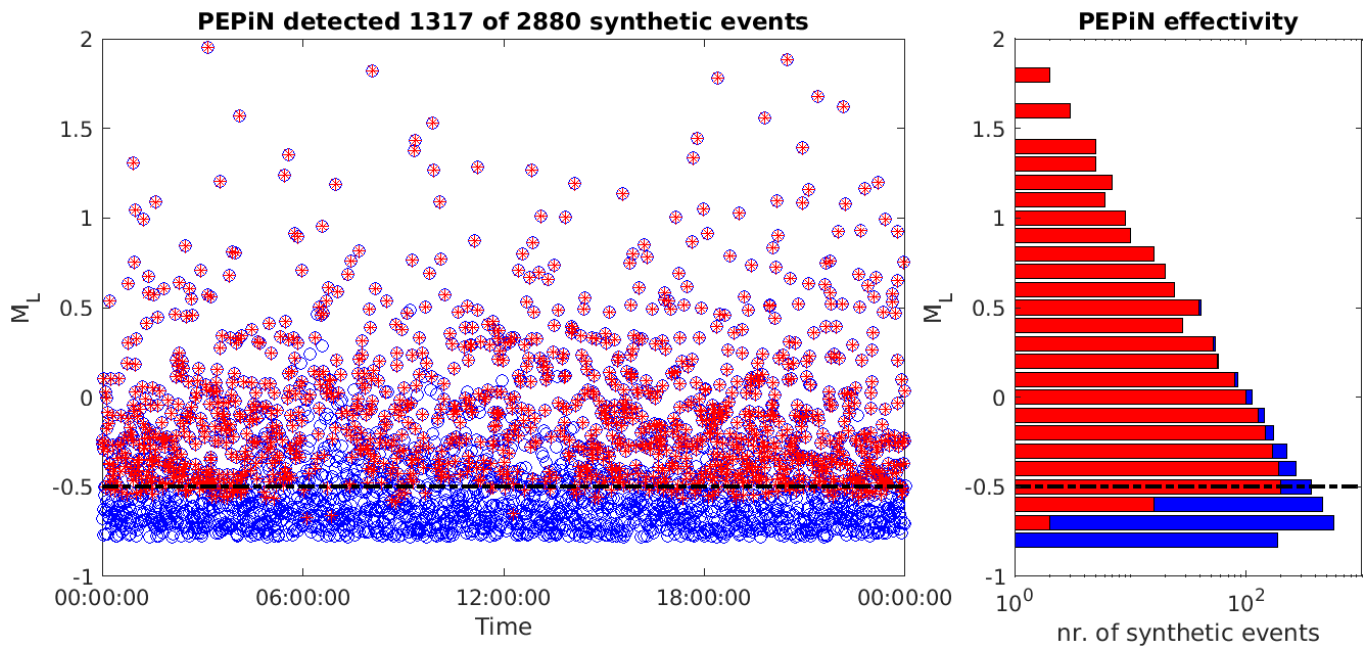


Figure 7 Detection results using 8 surface GRSN stations (left) Magnitude-time plot of all 2880 synthetic events (blue) and the 1317 detected by PEPiN (red) during a single day record with $-0.8 < M_L < 2.0$. The dashed black line indicates $M_C -0.5$. At least 4 S wave triggers were required; the M_L was converted from M_W using Eq. 4. (right) Gutenberg-Richter distribution of the events in (a).

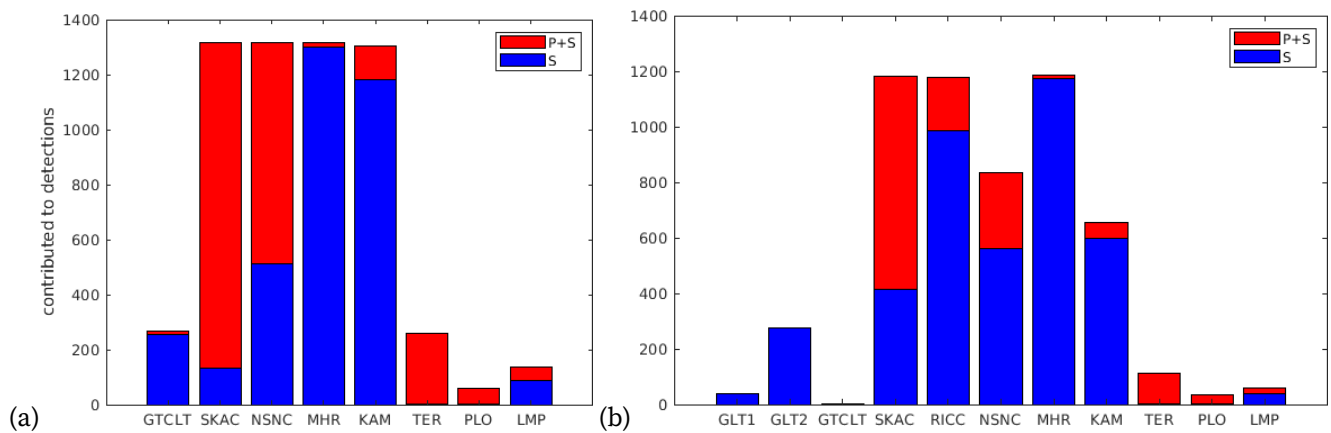


Figure 8 Efficiency of GRSN surface seismic stations, when 4 S waves are required to trigger: The rate at which individual stations contribute to event detection, when PEPiN utilizes 8 surface GRSN stations (a) or all 11 GRSN stations (b).

to wave arrivals on baserock stations (black waveforms). It is due to the greater velocities in the baserock velocity model which is used to create the synthetic seismograms of baserock stations.

4.3.1 Detection results: 8 surface stations

In the scenario involving 8 GRSN surface stations, PEPiN successfully detected 1317 out of 2880 synthetic earthquakes simulated with magnitudes ranging from $M_L -0.8$ to $M_L 2.0$, with no false triggers or duplicate detections of a single synthetic event observed. Analysis of the detection results, depicted in Fig. 7a, reveals a detection cutoff at magnitudes near $M_L -0.55$, with a few smaller events still being detected, and multiple stronger events ($M_L < 0.5$) remaining undetected during working hours (6:00 - 15:00). Magnitude completeness, estimated as $M_C -0.5$ (Fig. 7b), at which deviations

from the Gutenberg-Richter law are observed, is determined using the maximum curvature method (Wiemer and Wyss, 2000; Pavlenko and Zavyalov, 2022), which is akin to the approach employed in the study of network sensitivity (Káldy and Fischer, 2023).

Additionally, the test highlights the detection efficiency, revealing 0% detections missing above $M_L 0.5$, 12% at $M_L 0.0$, 24% at $M_L -0.3$ and 45% at $M_L -0.5$. The overall detection efficiency above magnitude of completeness $M_C -0.5$ is calculated to be 82%.

Upon closer examination of the GRSN efficiency, it becomes evident that all events (1303 out of 1317) would still be detected even if only the SKAC, NSNC, MHR, and KAM stations were available, as illustrated in Fig. 8a. Notably, these stations emerge as the most beneficial ones based on individual station sensitivity, as given in Káldy and Fischer (2023, Fig. in the supplement). In contrast, the other 4 stations - GTCLT, TER, PLO, and

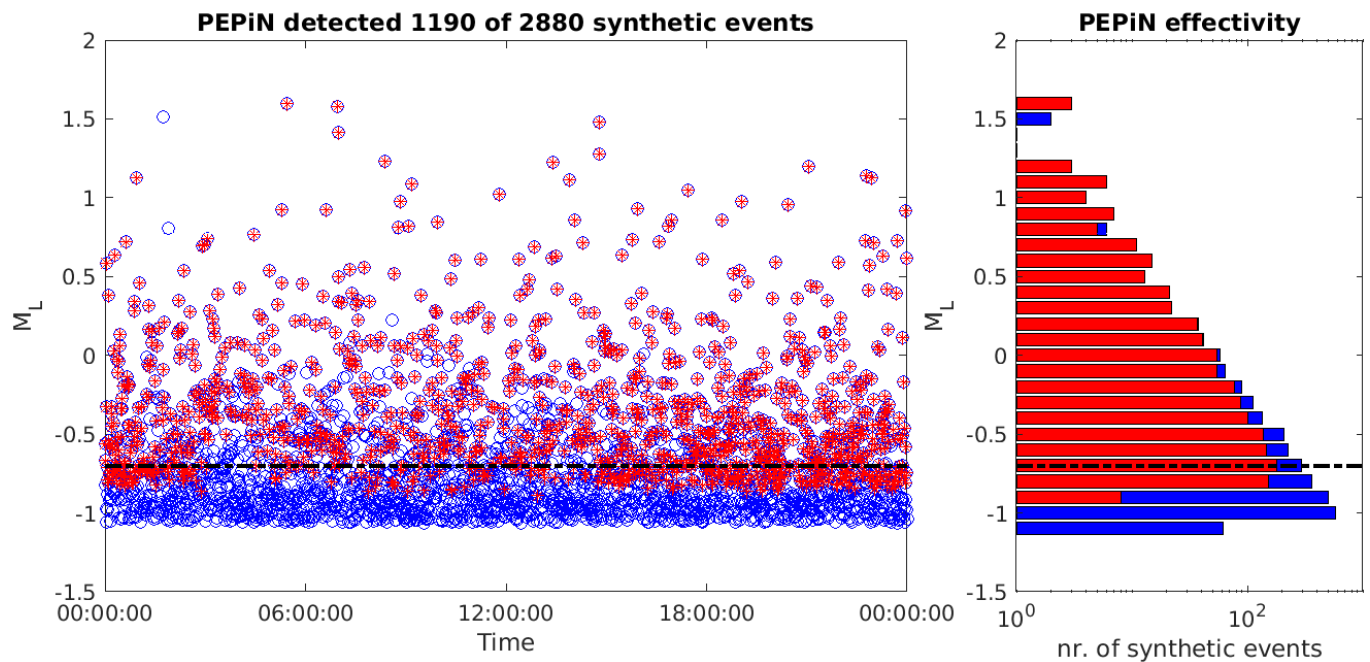


Figure 9 Detection results, similar to Fig. 7 using 11 GRSN stations. In this case, PEPiN detected 1190 earthquakes during a single day record of the total 2880 synthetic earthquakes with $-1.05 < M_L < 1.6$. Dashed black line points out M_C -0.7.

LMP - exhibit varying degrees of contribution, ranging from 60 to 267 event detections.

4.3.2 Detection results: 9 surface + 2 well stations

When PEPiN is configured to utilize all 11 GRSN stations, it successfully detected 1190 out of 2880 events with M_L from -1 to 2, achieving a magnitude of detection completeness M_C -0.7 (Fig. 9). Notably, two events with magnitudes M_L 1.5 and M_L 0.8 were missed by PEPiN, while the strongest synthetic event with a magnitude of M_L 1.76 was recognized by PEPiN as two separate events. Additionally, PEPiN generated a single false trigger during the detection process. The reason for two detections instead of a single strong event is that the first, stronger detection consisted of 11 correct picks on 6 stations, while the second, smaller detection incorporated 4 correct picks on 2 different stations plus 3 noise-triggers recognized as S picks (one at GLT1).

The detection patterns confirm the effect of the increased noise during working hours, but unexpectedly the strongest missed events occurred during the night (Fig. 9a). Overall, PEPiN utilizing 11 stations is missing 0% at M_L 0.5, 7% at M_L 0.0, 33% at M_L -0.5 and 40% at M_C . The overall efficiency of detection above M_C -0.7 is calculated to be 78%.

Closer examination of the station efficiency with all 11 GRSN stations utilized by PEPiN (Fig. 8b), it becomes evident that 3 stations (SKAC, RICC, and MHR) contribute significantly to all the detections, accounting for 1179 out of 1190 events. Additionally, the other 2 most beneficial stations, NSNC and KAM, play substantial but interchangeable roles by contributing to 70% and 55% of detections, respectively; which is a decline to their irreplaceable contribution in the 8 station setup, where they had to fully contribute to the requirement of 4 triggers. Interestingly, it is the shallower borehole stations

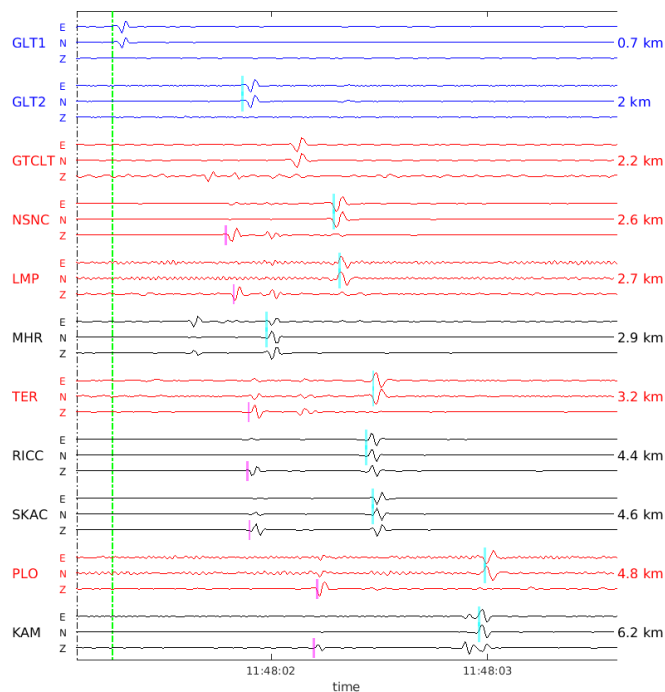


Figure 10 Waveforms of an event M_L 0.8 where all the synthetic signals exceed the real noise level. PEPiN P picks are shown in magenta, S picks in cyan and interpreted origin time by the green line. Seismograms in velocity, filter 7-30 Hz, individual scale per component. This event is located at x -0.75, y 0.61 and z 2.48 km.

GLT2 that are picked by PEPiN in 23% of the detected events. In contrast, the remaining 4 surface and the deep borehole stations contribute minimally to the detection process.

Furthermore, it is important to note that it is not the high noise levels that prevent PEPiN from assigning more picks to a single event. Fig. 10 shows a rel-

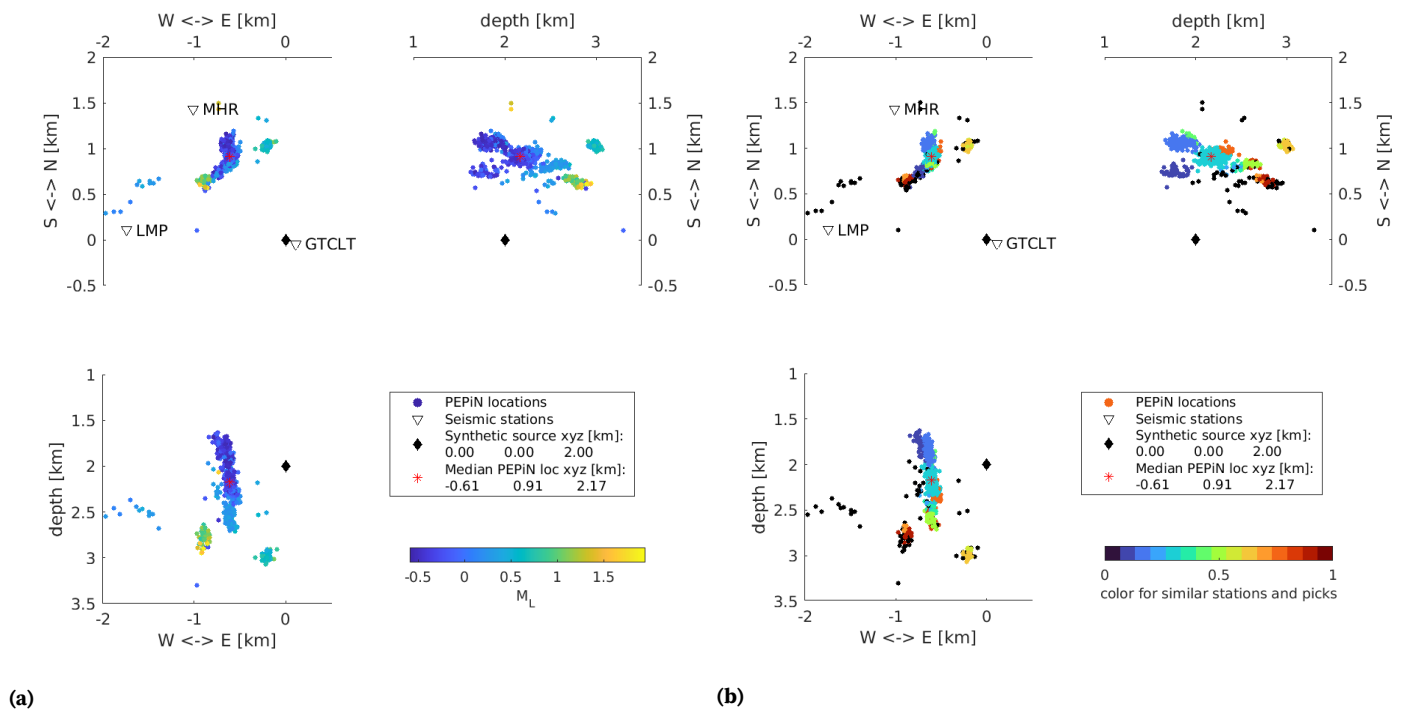


Figure 11 3D view of event locations using at least 1 P wave and 4 S wave picks at 8 surface stations. PEPiN detected 1317 out of 2880 events, located 1276 of them and 1253 locations are displayed here (the remaining are outside the displayed volume). Events in (a) are colored by magnitude, median location shown by the red star, and original location of the synthetic event by a black diamond. Point color in (b) identifies the events that were located using a similar set of picks; black points represent all groups with less than 10 events (mostly a single event). Origin [0, 0] of local coordinates is 50.5345N, 14.1535E, which is similar to synthetic event horizontal coordinates.

atively strong synthetic event with M_L 0.8, featuring 7 P picks and 9 S picks - the maximum number of picks across all detections. The reason for omitting clearly visible wave arrivals is related to the phase associator, which derives the maximum permitted time difference between S phases by assuming similar station altitude; this is not fulfilled in our case. Specifically, the down-hole stations GLT1, GLT2 (blue waveforms in Fig. 10) and the surface station GTCLT are separated 200 m horizontally, but up to 1500 m vertically. Therefore only one of them is allowed in an event.

4.4 Location efficiency

Over a thousand events were detected by PEPiN in both 8 and 11 station scenarios. If the station providing P and S picks surrounded the well of the planned EGS, the PEPiN location of detected events would be expected to cluster around the zero (local) coordinate and 2 km depth, because the synthetic events represent a single event in terms of waveform shape and arrival time. In this section, the locations of PEPiN with 8 surface and 9 surface + 2 borehole stations are discussed further.

Note that PEPiN detects both P and S signals (Fig. 8ab) on stations with favorable station correction (SKAC, MHR, Tab. 3), low noise level station (RICC is in an old underground mine) and on stations where the P wave signal is comparable to the S wave signal due to the focal mechanism (NSNC, TER, PLO and LMP, Fig. 5). Only the latter is expected to change in the real case scenario, which should not prevent PEPiN from making a location

due to lack of a P wave pick.

4.4.1 Location results: 8 surface stations

When utilizing only the 8 surface stations, the majority of detected events (1276 out of 1317) contain at least 1 P wave pick. Despite identical synthetic waveforms as the input, scaled and perturbed by real seismic background noise, the preliminary locations (Fig. 11) exhibit a fracture-like pattern. The median PEPiN location (depicted by the red star in Fig. 11) differs from the location of the synthetic earthquake (depicted by the black diamond) by 170 m in depth and 1.1 km horizontally.

Coloring the locations by event magnitude M_L (Fig. 11a) illustrates the relationship between magnitude and location, with each cluster in space exhibiting different magnitudes. Additionally, the clusters in space are differentiated by the set of picks used for their location (15 significant out of 63 groups colored, the rest remain black, Fig. 11b): Most events are located using a similar set of 4 stations - SKAC, NSNC, MHR, and KAM - varying in the station(s) at which the P wave is identified, primarily at NSNC and SKAC (Fig. 8a). All these contributing stations are located in NNW half space from the synthesized event, MHR being the closest to it, but not providing the P pick. The P-S pair is usually provided by stations of epicentral distance 1.5 - 4 km.

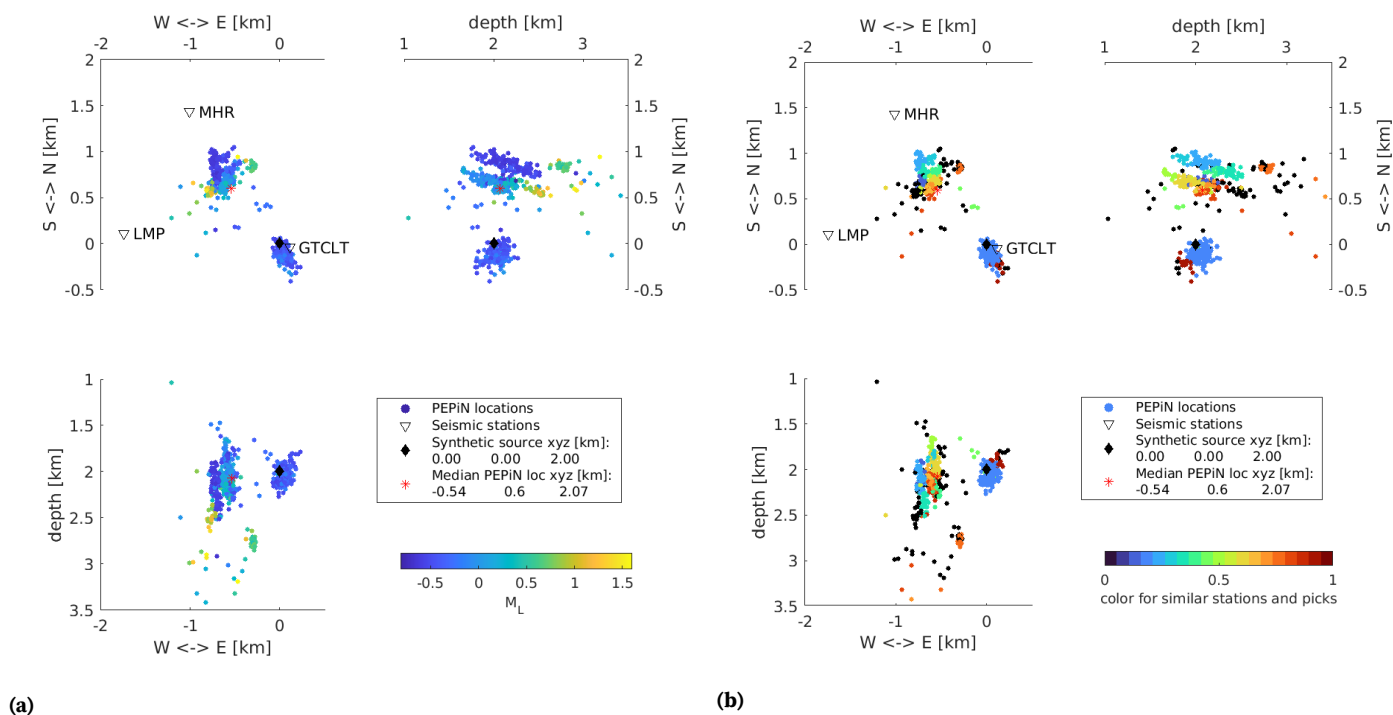


Figure 12 3D view of event locations, similar to Fig. 11 but PEPiN uses all 11 GRSN seismic stations: 1190 detected events, 850 of them located and 755 locations are displayed here (remaining are outside the area).

4.4.2 Location results: 9 surface + 2 well stations

When PEPiN utilizes all 11 stations, 805 out of 1190 detected events contain at least a single P wave pick. The preliminary locations (as shown in Fig. 12) exhibit significant clustering, overlapping the correct location in the case of one cluster. The median PEPiN location (depicted by the red star in Fig. 12) varies from the location of the synthetic earthquake (depicted by the black diamond) by 70 m in depth and 0.8 km horizontally.

Coloring the locations by event magnitude M_L (Fig. 12a) reveals that the strongest events are mostly located outside the major groups. Furthermore, the clusters in space are differentiated by the set of picks used for their location (18 significant out of 91 groups colored, while the rest remain black, Fig. 12b): The cluster of 349 events near the synthetic earthquake location (light blue in Fig. 12) is primarily located using the 4 baserock stations (only approx. 60 deg azimuthal coverage), with S wave picks from the deep borehole GLT1 station contributing to only 28 cases (Fig. 8b).

5 Summary and discussion

This study aimed to assess the theoretical sensitivity of the seismic network GRSN established in the seismically inactive Litoměřice region (Czech Republic), particularly in light of the increase in geothermal projects near urban areas. Since no local earthquakes were detected during years of monitoring, we created realistic synthetic seismograms of potential local earthquakes originating from one location near the planned geothermal well and merged them with real background noise. This way we simulated thousands of events per day to

evaluate the performance of the automated earthquake picker and locator PEPiN at the GRSN seismic network.

The theoretical sensitivity of the GRSN seismic network was already estimated by Káldy and Fischer (2023) using the mean seismic noise levels and seismic waves attenuation and it showed that noise and station correction plays a crucial role in a station's contribution to the overall sensitivity of the network, exceeding the role of distance from the source. In this paper we created nearly realistic synthetic seismograms of a local earthquake potentially occurring in the vicinity of the planned geothermal well to empirically test the network sensitivity on magnitude detection. Note that the complexity of synthetic seismograms is enhanced by using two different velocity models, simulating the stations located on either sedimentary layers or baserock. We scaled the seismograms to represent different earthquake magnitudes and merged them with real background noise seismograms, realistically simulating thousands of non-overlapping events per day. When the automated earthquake picker and locator PEPiN used seismograms from the same 8 stations as a challenge study (Káldy and Fischer, 2023), the resulting detection efficiency in terms of magnitude completeness was $M_L - 0.5$, being $M_L 0.2$ less optimistic than the simulated sensitivity. Such a difference is considered a proof of the previous theoretical study, especially when it is in the range of the magnitude uncertainty $M_L 0.2$ derived by Čermáková and Horálek (2015). Drawing such a conclusion from a single source mechanism and location has its limitations, even if this point is of the greatest importance. The poor geometry of the most efficient stations plays a significant role in that case where the focal mechanism causes the S wave signal to be weak in

the NN-W location; more extensive study could be conducted should the need arise.

When the detector used data for all of the GRSN stations, including 2 borehole ones, the network sensitivity rose to $M_C -0.7$, mostly due to the RICC station, which is located in an old underground limestone mine, currently used as a repository. The station has, in general, very low noise, except for occasional periods of construction activity in the repository, making the station's effect on the network sensitivity unstable. Surprisingly, the borehole seismic stations GLT1 and GLT2 (Fig. 8b) have a minimal effect for improving the detection or location capability. This is because the PEPiN associator is designed for surface seismic networks where there is no difference in the station altitudes. This effect is further amplified by the fact that the GLT1, GLT2 and GTCLT stations are located within a 200 m horizontal aperture but vary in depth significantly (1500, 190 and 0 m). The associator also missed strong events, which had an effect on the detection rate success - it decreased when 11 instead of 8 stations were used. This points to the need for modifying the PEPiN associator in future so that it accounts for the three-dimensional distance among the seismic stations, when there is significant variation in station altitudes.

Despite the similarity of synthetic events, the preliminary locations of both 8 and 11 station setups deviate by up to 1.5 km horizontally and 1 km in depth from the synthetic source, occasionally elongated in a form of a fault system (this should be considered for future seismic monitoring to avoid confusion between real fault and false fault system). Correct picks are generally obtained by PEPiN, albeit with occasional exceptions like the unusual S wave arrival at KAM (Fig. 10). Events are predominantly detected and located using arrival times at the baserock stations in the northwest and 1 station in the east, leading to an azimuthal gap resulting in systematic shifts in event locations and grouping epicenters in clusters with similar station sets used. Therefore we conclude that the location inaccuracies arise mainly from the insufficient azimuthal coverage of the contributing stations, being less from variations in station subsets utilized for localization, from noise interference, and from the different uniform velocity models applied.

We determined the magnitude of completeness M_C using the maximum curvature method (as published by Pavlenko and Zavyalov, 2022). The detector missed 40 (45%) of synthetic events at $M_C \pm 0.05$ and 24 (32%) at 0.2 above M_C . Overall, if the PEPiN picker and locator is applied, the GRSN seismic network has a 60% chance of detecting a potential induced earthquake of $M_L -0.7$ at a depth of 2 km, and a 97% chance it detects an earthquake of $M_L 0.0$ at the similar location. The sensitivity of seismic monitoring of the geothermal project in Litoměřice will be further improved by installing additional borehole sensors and by updating the phase associator.

Besides testing PEPiN efficiency and therefore the GRSN network sensitivity, this study has three other practical outputs: First, Green's functions and synthetic seismograms of local earthquakes were obtained. Second, we derived a 1D velocity model of sedimentary lay-

ers at the EGS site. Third, the table of station corrections, which now includes all GRSN stations, was extended.

The PEPiN algorithm has proved itself to be a valuable automated detector and locator of microseismic events, especially when the altitude of the stations is similar.

Acknowledgements

This manuscript received partial support from two projects: project *RINGEN - research infrastructure upgrade* No CZ.02.1.01/0.0/0.0/16_013/0001792, co-funded by the EU Operational Programme *Research, Development and Education* and project *SYNERGYS - systems for energy synergies* No CZ.10.02.01/00/22_002/0000172, co-funded by the EU Operational programme *Just Transition*.

The map in Fig. 1a was created using PYGMT.

We would like to thank the anonymous reviewers for their valuable comments and constructive suggestions, which helped to improve the quality of this article.

Data and code availability

Green's functions, which can be converted to synthetic seismograms for Bohemian Cretaceous Basin (sedimentary area) in Litoměřice, are available at: https://greens-mill.pyrocko.org/CZ_Litomeric_sediment_source2km_B-2c7ea7.

Competing interests

The authors have no competing interests.

References

- Allen, R. Automatic phase pickers: Their present use and future prospects. *Bulletin of the Seismological Society of America*, 72 (6B):S225-S242, 12 1982. doi: 10.1785/BSSA07206B0225.
- Allen, R. V. Automatic earthquake recognition and timing from single traces. *Bulletin of the Seismological Society of America*, 68(5): 1521-1532, 10 1978. doi: 10.1785/BSSA0680051521.
- Bachura, M. *The Structure of the West Bohemian Earthquake Swarm Source Zone*. Phd thesis, Institute of Hydrogeology, Engineering Geology and Applied Geophysics, Faculty of Science, Charles University, Prague, Czech Republic, April 2017. Available at <http://hdl.handle.net/20.500.11956/96104>.
- Burda, J., Lojka, R., Mlčoch, B., Valečka, J., and Žáček, V. Závěrečná zpráva za léta 2006-2007 geologické a hydrogeologické poměry ověřovacího vrtu pvgt-lt 1 v geotermální struktuře litoměřice pro energetické využití. Technical Report ČGS-Geofond: GF P123196, Česká geologická služba, 2008.
- Cajz, V., Rappich, V., Erban, V. and Pécskay, Z., and Radoň, M. Late Miocene volcanic activity in the České středohoří Mountains (Ohře/Eger Graben, northern Bohemia). *Geologica Carpathica*, 60(6):519-533, 2009. doi: 10.2478/v10096-009-0038-8.
- Chamberlain, C. J. and Townend, J. Detecting Real Earthquakes Using Artificial Earthquakes: On the Use of Synthetic Waveforms in Matched-Filter Earthquake Detection. *Geophysical Research Letters*, 45(21):11,641-11,649, 2018. doi: 10.1029/2018GL079872.

- Clarke, H., Eisner, L., Styles, P., and Turner, P. Felt seismicity associated with shale gas hydraulic fracturing: The first documented example in Europe. *Geophysical Research Letters*, 41(23):8308–8314, 2014. doi: 10.1002/2014GL062047.
- Deichmann, N. and Giardini, D. Earthquakes Induced by the Stimulation of an Enhanced Geothermal System below Basel (Switzerland). *Seismological Research Letters*, 80(5):784–798, 09 2009. doi: 10.1785/gssrl.80.5.784.
- Doubravová, J. and Horálek, J. Single Layer Recurrent Neural Network for detection of local swarm-like earthquakes—the application. *Geophysical Journal International*, 219(1):672–689, 07 2019. doi: 10.1093/gji/ggz321.
- Dubiński, J., Stec, K., and Bukowska, M. Geomechanical and tectonophysical conditions of mining-induced seismicity in the Upper Silesian Coal Basin in Poland: a case study. *Archives of Mining Sciences*, vol. 64(No 1):163–180, 2019. doi: 10.24425/ams.2019.126278.
- D’Alessandro, A., Luzio, D., D’Anna, G., and Mangano, G. Seismic Network Evaluation through Simulation: An Application to the Italian National Seismic Network. *Bulletin of the Seismological Society of America*, 101(3):1213–1232, 06 2011. doi: 10.1785/0120100066.
- Fischer, T. The August–December 2000 earthquake swarm in NW Bohemia: the first results based on automatic processing of seismograms. *Journal of Geodynamics*, 35(1):59–81, 2003a. doi: 10.1016/S0264-3707(02)00054-6.
- Fischer, T. Automatic location of swarm earthquakes from local network data. *Studia Geophysica et Geodaetica*, 47:83–98, 2003b. doi: 10.1023/A:1022251605990.
- Fischer, T., Hrubcová, P., Salama, A., Doubravová, J., Ágústsdóttir, T., Gudnason, E., Horálek, J., and Hersir, G. Swarm seismicity illuminates stress transfer prior to the 2021 Fagradalsfjall eruption in Iceland. *Earth and Planetary Science Letters*, 594:117685, 2022. doi: 10.1016/j.epsl.2022.117685.
- Geffers, G.-M., Main, I. G., and Naylor, M. Biases in estimating b-values from small earthquake catalogues: how high are high b-values? *Geophysical Journal International*, 229(3):1840–1855, 01 2022. doi: 10.1093/gji/ggac028.
- Gibbons, S. J. and Ringdal, F. The detection of low magnitude seismic events using array-based waveform correlation. *Geophysical Journal International*, 165(1):149–166, 04 2006. doi: 10.1111/j.1365-246X.2006.02865.x.
- Giudicepietro, F., Esposito, A. M., and Ricciolino, P. Fast Discrimination of Local Earthquakes Using a Neural Approach. *Seismological Research Letters*, 88(4):1089–1096, 05 2017. doi: 10.1785/0220160222.
- Grigoli, F., Cesca, S., Rinaldi, A. P., Manconi, A., López-Comino, J. A., Clinton, J. F., Westaway, R., Cauzzi, C., Dahm, T., and Wiemer, S. The November 2017 M_w 5.5 Pohang earthquake: A possible case of induced seismicity in South Korea. *Science*, 360(6392):1003–1006, 2018. doi: 10.1126/science.aat2010.
- Hallo, M. Microseismic Surface Monitoring Network Design - Sensitivity and Accuracy. art. cp-293-00307, 2012. doi: 10.3997/2214-4609.20148336.
- Hanks, T. C. and Kanamori, H. A moment magnitude scale. *Journal of Geophysical Research: Solid Earth*, 84(B5):2348–2350, 1979. doi: 10.1029/JB084iB05p02348.
- Heimann, S., Kriegerowski, M., Isken, M. P., Cesca, S., Daout, S., Grigoli, F., Juretzek, C., Megies, T., Nooshiri, N., Steinberg, A., Sudhaus, H., Vasyura-Bathke, H., Willey, T., and Dahm, T. Pyrocko - An open-source seismology toolbox and library. *Potsdam: GFZ Data Services*, 2017. doi: 10.5880/GFZ.2.1.2017.001.
- Heimann, S., Vasyura-Bathke, H., Sudhaus, H., Isken, M. P., Kriegerowski, M., Steinberg, A., and Dahm, T. A Python framework for efficient use of pre-computed Green’s functions in seismological and other physical forward and inverse source problems. *Solid Earth*, 10(6):1921–1935, 2019. doi: 10.5194/se-10-1921-2019.
- Heimann, S., Kriegerowski, M., Isken, M., Vasyura-Bathke, H., Cesca, S., Nooshiri, N., Petersen, G., Metz, M., Steinberg, A., Sudhaus, H., , and Dahm, T. Pyrocko - A Versatile Software Framework for Seismology. *EGU General Assembly 2020, Online*, pages EGU2020–18734, 2020. doi: 10.5194/egusphere-egu2020-18734, 2020.
- Horálek, J. and Šílený, J. Source mechanisms of the 2000 earthquake swarm in the West Bohemia/Vogtland region (Central Europe). *Geophysical Journal International*, 194(2):979–999, 05 2013. doi: 10.1093/gji/ggt138.
- Institute of Geophysics, Academy of Sciences of the Czech Republic. West Bohemia Local Seismic Network, 1991. doi: 10.7914/S-N/WB.
- Jakoubková, H. *Earthquake swarms in diverse tectonic environments: West Bohemia and Southwest Iceland*. Phd thesis, Institute of Hydrogeology, Engineering Geology and Applied Geophysics, Faculty of Science, Charles University, Prague, Czech Republic, September 2018. Available at www.ig.cas.cz/wp-content/uploads/2018/09/2018-jakoubkova-phd.pdf.
- Janská, E. and Eisner, L. Ongoing seismicity in the Dallas-Fort Worth area. *The Leading Edge*, 31(12):1462–1468, 2012. doi: 10.1190/tle31121462.1.
- Kasza, Z., Tonka, P., Szucs, P., Prohaszka, A., Szucs, P., Meszaros, F., and Szogoth, G. Závěrečná zpráva za léta 2006-2007 geologické a hydrogeologické poměry ověřovacího vrtu pvgt-lt 1 v geotermální struktuře litoměřice pro energetické využití. Technical Report 2007\Litomerice\Litomerice_1114fuzott.prj, Geo-Log Environmental Protection and Geophysical Ltd, 2007.
- Kennett, B. L. N. and Furumura, T. Significant P wave conversions from upgoing S waves generated by very deep earthquakes around Japan. *Progress in Earth and Planetary Science*, 6(1):49, 2019. doi: 10.1186/s40645-019-0292-z.
- Kraft, T. and Deichmann, N. High-precision relocation and focal mechanism of the injection-induced seismicity at the Basel EGS. *Geothermics*, 52:59–73, 2014. doi: 10.1016/j.geothermics.2014.05.014.
- Kraft, T., Roth, P., and Wiemer, S. Good-Practice Guide for Managing Induced Seismicity in Deep Geothermal Energy Projects in Switzerland (Version 2), 11 2020. doi: 10.3929/ethz-b-000453228.
- Káldy, E. and Fischer, T. Microseismic network sensitivity in case of no seismic activity. *Journal of Seismology*, 27(4):627–641, 2023. doi: 10.1007/s10950-023-10134-y.
- Leptokarpoulos, K. and Gkaraouni, C. A magnitude independent space-time earthquake clustering algorithm (MISTIC). *Bulletin of the Geological Society of Greece*, 50(3):1359–1368, Jul. 2016. doi: 10.12681/bgsg.11849.
- Leptokarpoulos, K. M., Adamaki, A. K., Roberts, R. G., Gkaraouni, C. G., and Paradisopoulou, P. M. Impact of magnitude uncertainties on seismic catalogue properties. *Geophysical Journal International*, 213(2):940–951, 01 2018. doi: 10.1093/gji/ggy023.
- Levin, B., Sasorova, E., Borisov, S., and Borisov, A. Estimating the parameters of small earthquakes and their signals. *Journal of Volcanology and Seismology*, 4(3):203–212, 2010. doi: 10.1134/S074204631003005X.
- López-Comino, J., Cesca, S., Kriegerowski, M., Heimann, S., Dahm, T., Mirek, J., and Lasocki, S. Monitoring performance using synthetic data for induced microseismicity by hydrofracking at the Wysin site (Poland). *Geophysical Journal International*, 210(1):

- 42–55, 04 2017. doi: 10.1093/gji/ggx148.
- Magotra, N., Ahmed, N., and Chael, E. Seismic event detection and source location using single-station (three-component) data. *Bulletin of the Seismological Society of America*, 77(3):958–971, 06 1987. doi: 10.1785/BSSA0770030958.
- Magrini, F., Jozinović, D., Cammarano, F., Michelini, A., and Boschi, L. Local earthquakes detection: A benchmark dataset of 3-component seismograms built on a global scale. *Artificial Intelligence in Geosciences*, 1:1–10, 2020. doi: 10.1016/j.aiig.2020.04.001.
- Majer, E., Tait, A., and Wong, I. Protocol for addressing induced seismicity associated with enhanced geothermal systems. Technical Report DOE/EE-0662, U.S. Department of Energy, Energy Efficiency Renewable Energy, 01 2012. https://www.researchgate.net/publication/221678264_Protocol_for_addressing_induced_seismicity_associated_with_enhanced_geothermal_systems#fullTextFileContent.
- Muntendam-Bos, A. and Grobbe, N. Data-driven spatiotemporal assessment of the event-size distribution of the Groningen extraction-induced seismicity catalogue. *Scientific Reports*, 12: 10119, 2022. doi: 10.1038/s41598-022-14451-z.
- Myslil, V., Stibitz, M., Frydrych, V., and et al. Geotermální vrtné ověření struktury litoměřice pro energetické využití: Závěrečná zpráva o řešení projektu v programu trvalá prosperita mpo v roce 2006 - 2007. Technical Report Ev.č. projektu: 2A-1TP1/043, Geomedia, 2007.
- Myslil, V., Karous, M., Pačes, T., and et al. Geothermal project for the Litoměřice heating plant. Technical report, Geotern s.r.o., 2012.
- Mysliveček, J., Rapprich, V., Kochergina, Y. V., Magna, T., Halodová, P., Pécskay, Z., and Poňavič, M. Petrology of weakly differentiated alkaline, high-level intrusive rocks in the Zahofány-Chotiněves Belt near Litoměřice (Czech Republic). *Journal of Geosciences*, 63(4):317–331, 2018.
- Nolte, K. A. and Tsoulias, G. P. Identifying Direct *i*-Converted Waves Constrains Local Induced Earthquake Depths. *Seismological Research Letters*, 92(6), 07 2021. doi: 10.1785/0220200385.
- Pavlenko, V. and Zavyalov, A. Comparative Analysis of the Methods for Estimating the Magnitude of Completeness of Earthquake Catalogs. *Izvestiya, Physics of the Solid Earth*, 58, 2022. doi: 10.1134/S1069351322010062.
- Perol, T., Gharbi, M., and Denolle, M. Convolutional neural network for earthquake detection and location. *Science Advances*, 4(2): e1700578, 2018. doi: 10.1126/sciadv.1700578.
- Rosenberger, A. Real-Time Ground-Motion Analysis: Distinguishing P and S Arrivals in a Noisy Environment. *Bulletin of the Seismological Society of America*, 100(3):1252–1262, 06 2010. doi: 10.1785/0120090265.
- Shearer, P. M. *Introduction to Seismology*. Cambridge University Press, 2009.
- Stepnov, A., Chernykh, V., and Konovalov, A. The Seismo-Performer: A Novel Machine Learning Approach for General and Efficient Seismic Phase Recognition from Local Earthquakes in Real Time. *Sensors*, 21(18), 2021. doi: 10.3390/s21186290.
- Uličný, D., Laurin, J., and Čech, S. Controls on clastic sequence geometries in a shallow-marine, transtensional basin: the Bohemian Cretaceous Basin, Czech Republic. *Sedimentology*, 56 (4):1077–1114, 2009. doi: 10.1111/j.1365-3091.2008.01021.x.
- Velasco, A. A., Alfaro-Díaz, R., Kilb, D., and Pankow, K. L. A Time-Domain Detection Approach to Identify Small Earthquakes within the Continental United States Recorded by the USArray and Regional Networks. *Bulletin of the Seismological Society of America*, 106(2):512–525, 04 2016. doi: 10.1785/0120150156.
- Wang, R. A simple orthonormalization method for stable and efficient computation of Green's functions. *Bulletin of the Seismological Society of America*, 89(3):733–741, 06 1999. doi: 10.1785/BSSA0890030733.
- Wang, R., Heimann, S., Zhang, Y., Wang, H., and Dahm, T. Complete synthetic seismograms based on a spherical self-gravitating Earth model with an atmosphere–ocean–mantle–core structure. *Geophysical Journal International*, 210(3):1739–1764, 06 2017. doi: 10.1093/gji/ggx259.
- White, J. A. and Foxall, W. Assessing induced seismicity risk at CO2 storage projects: Recent progress and remaining challenges. *International Journal of Greenhouse Gas Control*, 49:413–424, 2016. doi: 10.1016/j.ijggc.2016.03.021.
- Wiemer, S. and Wyss, M. Minimum Magnitude of Completeness in Earthquake Catalogs: Examples from Alaska, the Western United States, and Japan. *Bulletin of the Seismological Society of America*, 90(4):859–869, 08 2000. doi: 10.1785/0119990114.
- Wilson, D. C., Wolin, E., Yeck, W. L., Anthony, R. E., and T., R. A. Modeling seismic network detection thresholds using production picking algorithms. *Seismological Research Letters*, 93(1): 149–160, 2021. doi: 10.1785/0220210192.
- Yang, W., Chen, G., Meng, L., Zang, Y., Zhang, H., and Li, J. Determination of the local magnitudes of small earthquakes using a dense seismic array in the Changning–Zhaotong Shale Gas Field, Southern Sichuan Basin. *Earth and Planetary Physics*, 5 (6):epp2021026, 2021. doi: 10.26464/epp2021026.
- Čermáková, H. and Horálek, J. The 2011 West Bohemia (Central Europe) earthquake swarm compared with the previous swarms of 2000 and 2008. *Journal of Seismology*, 19(4):899–913, 2015. doi: 10.1007/s10950-015-9502-3.
- Šafanda, J., Verner, K., Franěk, J., Peřestý, V., Holeček, J., and Fischer, T. Geology and geothermal potential in the eastern flank of Eger Rift (Litoměřice area, Czech Republic). *Geothermics*, 86: 101808, 2020. doi: 10.1016/j.geothermics.2020.101808.

The article *Performance of an Automatic Detector and Locator Tested on Synthetic Seismograms - A Case Study from Litoměřice in Czech Republic* © 2025 by Eva Káldy is licensed under CC BY 4.0.